Effect of the clay and the metal container in retaining Sm^{3+} and ZrO^{2+} and the reversibility of the process.

SAID EL MRABET[1], MIGUEL A. CASTRO[1], SANTIAGO HURTADO[2], M. MAR ORTA[1], M. CAROLINA PAZOS[3], MARÍA VILLA-ALFAGEME[4], AND MARÍA D. ALBA[1,†]

[1] Instituto Ciencia de Materiales de Sevilla (CSIC-Universidad de Sevilla).

Avda. Américo Vespucio, 49. 41092 Sevilla, Spain.

[2] Servicio de Radioisótopo del CITIUS (Universidad de Sevilla).

Avda. Reina Mercedes, 4. 41012 Sevilla, Spain.

[3] Escuela de Ciencias Químicas, Universidad Pedagógica y Tecnológica de Colombia UPTC.

Avda. Central del Norte, Vía Paipa, Tunja, Boyacá, Colombia

[4] Dpt. Física Aplicada II (Universidad de Sevilla).

Avda. Reina Mercedes, s/n. 41012 Sevilla, Spain.

ABSTRACT

Knowledge and understanding about radionuclides retention processes on the materials composing the engineered barrier (clay mineral and metallic container waste) are required to ensure the safety and the long-term performance of radioactive waste disposal. Therefore, the present study focuses on the competitiveness of clay and the metallic container in the process of adsorption/desorption of the radionuclides simulators of Am^{3+} and UO_2^{2+}. For this purpose, a comparative study of the interaction

† *Corresponding author: TEL: +34 954489546*
E-mail: alba@icmse.csic.es

of samarium (chosen as chemical analogue for trivalent americium) and zirconyl (as simulator of uranyl and tetravalent actinides) with both FEBEX bentonite and metallic container, under subcritical conditions, was carried out. The results revealed that the AISI-316L steel container, chemical composition detailed on Table 1, immobilized the HRW, even during the corrosion process. The ZrO^{2+} was irreversibly adsorbed on the minireactor surface. In the case of samarium SEM/EDX analysis revealed the formation of an insoluble phase of samarium silicate on the container surface. There was no evidence of samarium diffusion through the metallic container. Samarium remained adsorbed by the container also after desorption experiment with water. Therefore, steel canister is actively involved in the HRW immobilization.

Keyword. geological disposal, metallic canister, clay minerals, radionuclide waste, actinide, sorption/desorption.

INTRODUCTION

The safe disposal of radioactive wastes and specifically the need to protect humans and the environment in the far future is given particular attention in all countries engaged in nuclear power generation. Nowadays, disposal of these wastes in deep geological repositories has been established as the safest and the most environmentally appropriate solution (Alba et al., 2005; Duro et al., 2008; Alba et al., 2009). Repositories are generally designed on the basis of a multiple barrier system which consists mainly of natural and engineered barriers to isolate the hazardous radionuclides from the accessible environment (McCombie et al., 2000; Astudillo, 2001; Chapman, 2006). The engineered barrier system (EBS) comprises the respective metallic containers filled with radioactive waste and a backfill clay material, mostly smectite standing between container and host rock in order to avoid the access of groundwater to the high radioactive waste (HRW) as well as its subsequent migration out of repository (Malekifarsani et al., 2009). However, it is impossible to guarantee the long-term stability and integrity of the engineered barrier system. Once the overpack comes into contact with groundwater higher concentrations of CO_3^{2-} ions (Ishidera et al., 2008), it will begin to corrode and, therefore, smectite could interact with dissolved iron, hydrogen gas and other corrosion products of the steel overpack such as magnetite (Fe_3O_4), goethite (FeO(OH)) (Smart et al., 2002; Carlson et al. 2007) or siderite.

Therefore, the corrosion of candidate metals for the container as well as the effect of their corrosion products with clay minerals were the subject of many experimental investigations and geochemical modelling (Guillaume et al., 2003; Papillon et al., 2003; Perronnet, 2004; Wilson et al., 2006b; Bildstein et al., 2006). Studies of iron-clay interactions have shown the systematic destabilization of the initial

clay mineral and the subsequent crystallization of reaction products (Guillaume et al., 2003, 2004; Lantenois et al., 2005). Lantenois et al. (2003) has investigated the interactions between Fe and a variety of natural and synthetic smectite samples with the aim of determining the effect of crystallo-chemical features on the smectite/iron interactions. At 80°C, the results indicated that oxidation of the container by smectites occurs only for dioctahedral smectites under basic pH conditions, whereas the container corrodes by precipitating magnetite, but without smectite alteration at pHs ranging from slightly acid to neutral. Likewise, Wilson et al. (2006a; 2006b) has investigated the stability of Na-montmorillonite between 80ºC and 250ºC and observed that Fe-rich smectite was formed and they exhibited lower swelling properties than the Na-montmorillonite. Moreover, at 250ºC, berthierine was formed.

All these previous studies showed that the effect of container corrosion on the stability of the clay depends on many parameters such as temperature or the nature of the clay minerals. In addition, a geochemical modelling study of iron/clay interactions has been conducted by Samper et al. (2008) and demonstrated that most of the Fe diffuses from the canister into the clay, where it sorbs or precipitates as magnetite. Moreover, as reported in previous study, this magnetite is expected to act as sorbing layer and it is able to delay the diffusion and immobilise many radionuclides under repository conditions (Tiziana Missana et al., 2003). Indeed, several studies have been undertaken to determine the ability of magnetite, commonly formed on corroding steel surfaces, to absorb or reduce some radionuclides (Granizo and Missana, 2006; Rovira et al., 2004). El Amrani et al. (2007) studied sorption of uranium onto magnetite and found that the sorbed uranium is a mixture of tetra- and hexa-valent uranium.

In light of these studies, an understanding of the sorption/retention of radionuclides on materials composing the engineered barrier (clay and metallic

container waste) is of paramount importance for the long-term performance assessment of nuclear waste repositories. El Mrabet. et al. (2012) have carried out experiments to study the competitive effect of the steel canister and clay barrier on the sorption of Eu^{3+} used as trivalent actinides under reducing conditions and reported that both components of the engineering barrier (clay mineral and metallic canister) were involved in the immobilization of Eu^{3+} by the formation of insoluble europium silicate phases. However, to our knowledge, it is unclear whether this behaviour is general for any actinide in trivalent or other oxidation states. Therefore, the present study focuses on the competitiveness of clay and the steel container in the process of adsorption/desorption of the radionuclide simulators of Am^{3+} and UO_2^{2+}. For this purpose, chemical analogue simulators were chosen; Sm^{3+} as simulator of trivalent Am and zirconyl as simulator of uranyl and tetravalent actinides. The FEBEX bentonite was selected as simulator of the materials of the engineered barrier and the austenitic stainless steel AISI-316L as simulator of the metallic material.

EXPERIMENTAL METHODS

Experimental design and materials.

The clay mineral used in this study (Bentonite FEBEX) has been extensively investigated as a suitable component of the engineered barrier in the recent past in many countries in Europe and around the world (Triphaty et al., 2004). This bentonite was provided by the ENRESA Company (the Spanish Company in charge of radioactive wastes management) and has the structural formula: $(Ca_{0.5}Na_{0.08}K_{0.11})(Si_{7.78}Al_{0.22})(Al_{2.78}Fe^{3+}_{0.33}Fe^{2+}_{0.02}Mg_{0.81})O_{20}(OH)_4$. Its main phase is

montmorillonite (smectite percentage higher than 90%) together with small amounts of quartz (Fernandez et al., 2004).

$Sm(NO_3)_3 \cdot 6H_2O$ and $ZrO(NO_3)_2 \cdot 7H_2O$ which are commercially available from Sigma-Aldrich, were used in this work as possible chemical analogues for long-lived actinides present in HRW, Sm as simulator of trivalent Am and zirconyl as simulator of uranyl and tetravalent actinides (Chapman and Smellie, 1986).

Copper, titanium, stainless steels, were chosen in a number of disposal concepts as suitable materials for the canisters. Also, they exhibit a high attack resistance in the expected disposal environment (Rebak, 2006). Therefore, in the present study, hydrothermal experiments were carried out in a stainless steel AISI-316 L reactor, (selected as candidate container), commercially available, the chemical composition is given in Table 1.

A deep understanding of the competitive effect of the canister material in the processes by which the bentonite retains radioactive waste is of great importance for the long term stability of the engineered barrier system. For this purpose, a minireactor made from the same material as the steel reactor was designed by us. Thus, 300 mg of the powdered bentonite was placed into a cylindrical steel cell (minireactor). The bentonite-minireactor set was then compacted in a cylindrical die, (experimental design has been described in detail by El Mrabet et al., 2012). Finally, the compacted set was placed into the steel reactor and submitted to a hydrothermal treatment. The hydrothermal reactions were carried out with 7.9×10^{-2} M of each solution of Sm^{3+} or ZrO^{2+} at 300ºC for 4.5 days.

Despite of the expected temperature in the disposal repositories will not exceed 150ºC, many studies have been carried out by simulating the deep geological disposal at temperatures up to 350ºC to increase the reaction rate (Mathers et al., 1982; Savage and

Chapman, 1982; Allen et al., 1988, Alba and Chain., 2007). Therefore, in the present study, higher temperatures were taken account as necessary conditions to increase the reaction rate and run the experiments at laboratory scale.

Desorption study was carried out by washing both treated minireactors with distilled water until the washed water reached a neutral pH.

Characterization methods.

The X-ray diffraction patterns were obtained using an X'Pert Pro PANALYTICAL diffractometer in the conventional $\theta - 2\theta$ Bragg–Brentano configuration using Cu Kα radiation. Diffragtograms were registered from 3º to 70º 2θ and in steps of 0.05º in random powder mode.

The morphology and chemical composition of both the steel and clay mineral before and after hydrothermal treatment with the Sm^{3+} or ZrO^{2+} solution at 300ºC for 4.5 days were investigated using a SEM-FEG HITACHI S- 4800 a scanning electron microscope equipped with an Xflash 4010 (BRUKER) for energy dispersive X-ray (EDX) analysis. The EDX spectra were taken in point analysis mode.

In order to obtain useful information about the oxide scale structure, a detailed cross-sectional study involving SEM observations in combination with EDX line profile along a representative area of the minireactor was performed.

The pH and Eh of the supernatant were measured at room temperature using a Eutech Instruments PC 700 pH-meter before and after the hydrothermal treatment in aerobic conditions.

RESULTS

Sorption of Sm^{3+} on the FEBEX smectite

The XRD pattern of untreated clay mineral (Fig. 1a) exhibited typical reflections of montmorillonite with a series of narrow and sharp peaks indicating its crystalline structure. The basal spacing d_{001} which corresponds to a value of about 1.4 nm is associated to the bilayer hydrated Ca^{2+} in the smectite clay interlayer (Chain, 2007). Additionally, the XRD showed narrow peaks that correspond to quartz (PDF 04-006-1757) and cristobalite (PDF 04-008-7824). After hydrothermal treatment with Sm^{3+} (Fig. 1b), the montmorillonite remains as the main constituent of the clay mineral and the quartz is now absent but new impurities, $H_2Si_2O_5$ (PDF 00-050-0439) and Nacrite-2M2 (PDF 01072-2206), are observed. The strongest peak that appears at 2θ value of 6.33º, which corresponds to [001] lattice plane, shifted after hydrothermal treatment to a lower diffraction angle 5.84º, thus implying an increase in basal spacing d_{001} which may be attributed to the sorption of hydrated M^{3+} cations into the interlayer space (Alba et al., 2001). Previous studies demonstrated that the hydrothermal treatment of clay minerals in the presence of the canister does not provoke a decreasing of its swelling capacity, (Bildstein et al, 2006; Carlson et al., 2007; Gaudin et al., 2009; Savage et al., 2010). The 060 reflection of FEBEX does not change after hydrothermal treatment and was found to be 0.149 nm as expected for dioctahedral smectites (Davitz and Low, 1970).

The SEM micrographs of FEBEX before and after hydrothermal treatment with Sm^{3+} at 300ºC for 4.5 days are shown in (Fig.2). The untreated clay showed the lamellar morphology for the most particles (Fig. 2a). Furthermore, the typical $K_{\alpha 1}$ lines for Si,

Mg, Al and Ca in montmorillonite can be seen in the corresponding EDX spectrum, (Fig. 2d). In the case of the reacted clay mineral with Sm^{3+}, the most particles exhibited a lamellar morphology as can be seen in Fig. 2b, the associated EDX spectrum (Fig. 2e) showed the typical $K_{\alpha 1}$ lines for Si, Mg and Al of FEBEX, $L_{\alpha 1}$ and $L_{\beta 1}$ lines of Sm which indicated that Sm was absorbed in the interlayer space of the FEBEX bentonite. The decrease of the Mg content and the absence of Ca when compared to the original FEBEX are due to the leaching of Mg^{2+} ions and the exchange of Ca^{2+} by Sm^{3+} in the interlayer space, which is in accordance with the observed lamellar expansion by XRD. Besides those lamellar particles, some compact block particles (Fig. 2c, ①) were also observed with chemical composition associated to the phases containing samarium which were not detected by XRD (Figs. 2f). It should be noted that the presence of chromium is due to the degradation of the minireactor (see the chemical composition of the steel reactor in Table 1).

Sorption of Sm^{3+} on the minireactor.

The XRD patterns of the minireactor after hydrothermal treatment at 300ºC for 4.5 days in contact with a solution of Sm^{3+} $7.9x10^{-2}$ M (Fig. 3a) showed that the original austenitic metallic matrix of the steel (see it chemical composition in Table 1) remains as the dominating phase. Additionally, a considerable portion of phases containing iron (goethite) from container degradation marked by ② as well as other phases containing samarium marked by①, ③ and ④ were also observed. Under scanning electron microscopy, the surface of the reactor appears to be entirely covered by a thin layer of oxide (Fig. 4a). The EDX spectrum showed the spectral lines of the austenitic phase together with Sm peaks (Fig. 4g).

After hydrothermal reaction with FEBEX and Sm^{3+} solution, (Fig. 3b), the dominant peaks in the X-ray diffraction pattern of the minireactor corresponds to the original austenitic phase. Furthermore, minor phases such as samarium aluminate ($SmAlO_3$, PDF 00-22-1307), samarium oxide (Sm_2O_3, PDF 01-076-0153) and clinozoisite ($Ca_2Al_3(SiO4)(Si_2O_7)O(OH)$, PDF 00-44-1400) which contains elements leached from the clay mineral were also detected. As can be seen by SEM micrographs, Fig. 4b, a homogeneous compact thin layer formed by small crystals covers the entire surface of the reactor. According to the EDX analysis, the higher Sm/Si ratio together with weak intensity of K_α lines of Al and Mg arising from clay minerals particles implies that the thin layer of oxide was Si- and Sm- rich, (Fig. 4h). The thickness of this layer is corroborated by the maintenance of Cr/Fe intensity ratio in the EDX spectra, (Figs. 4f-4h). Beside this, some compact block particles (Fig. 4c, ①) with a chemical composition associated with samarium silicate were also observed (Figs. 4i).

In order to get a deeper insight about the diffusion of samarium into the minireactor and the distribution of the chemical elements in the oxide layer formed after hydrothermal reaction, a cross-sectional study involving SEM observations combined with EDX line profile along a representative area (white line in Fig. 5a) of the minireactor was performed. This study showed that the oxide scale is thin and mainly composed of samarium silicate at the scale-atmosphere interface (Fig. 5b). There was no evidence of samarium diffusion towards the metallic container, which is in accordance with the results obtained by surface EDX analysis.

Desorption of Sm^{3+} on the minireactor.

When the steel was submitted to desorption process after hydrothermal treatment, the identified species by XRD pattern (Fig. 3c) are the same as those seen previously in the reactor post-treatment. Nevertheless, the top surface morphology of the oxide scale formed over the steel changes significantly when comparing to that of the reactor post-treatment. SEM micrographs showed that the minireactor surface is covered by a fine-grain oxide layer intercalated in some areas by a very thin layer of samarium silicate (Figs. 4d-4j). Besides this, agglomerations of small particles (Fig. 4e, ②) were also observed with a chemical composition compatible with samarium silicate as stated by EDX spectrum (Figs. 4k). However, as can be seen in Figs. 5c-5d, the cross sectional study of the reactor hardly revealed the presence of samarium silicate whose thickness has been significantly reduced with respect to the reactor post-treatment.

Sorption of ZrO^{2+} on the FEBEX smectite

The XRD patterns of the reacted clay FEBEX with a solution of ZrO^{2+} $7.9x10^{-2}$ M at 300ºC for 4.5 days, (Fig. 6b) showed that the basal spacing d_{001} expanded from 1.40 nm to 1.46 nm, suggesting that the interlayer cation exchange between the initial (Ca^{2+} and Na^{+}) by ZrO^{2+} has been occurred. Also, the persistence of the d- spacing of 1.49 nm peak without any reflection to a higher 2θ angle indicated no leaching of the octahedral cations. It can also be noticed form XRD analysis that neither phases resulting from minireactor degradation, nor those containing zirconium were detected in the treated clay minerals, which is probably due to their small crystalline size. SEM micrographs of the reacted FEBEX with ZrO^{2+} showed the typical lamellar morphology for the most of particles with a chemical composition compatible with ZrO^{2+}as interlayer cations, (Figs. 7a-7d). In addition to these lamellar particles and under

backscattering electron beam, agglomerations of small particles with brilliant appearance (Fig. 7b, ①) were also observed with a chemical composition consisting mainly of phase containing zirconium, (Figs. 7e). Moreover, the SEM/EDX analysis of other zone (labelled ② in Fig. 7c) indicated that the treated clay mineral was significantly enriched in iron, which suggested the release of the iron upon degradation of the container, (Figs. 7f).

Finally, it is remarkable that the corresponding EDX spectra were characterised by the $K_{\alpha 1}$ lines of Si, Al, Mg and L_{α} line of Zr. Thus, there was no evidence of the existence of isolated zirconium silicate, the zirconium being associated to the clay mineral phase. Similar observations were seen in the case of the treated clay with Sm^{3+}.

Sorption of ZrO^{2+}on the minireactor

The XRD patterns of the minireactor treated hydrothermally at 300ºC for 4.5 days in contact with a solution of ZrO^{2+} $7.9x10^{-2}$ M (Fig. 8a) showed the austenite as the dominating metallic phase of the steel which suggested that the minireactor did not undergo any noticeable change in term of phase transformation due to the hydrothermal treatment. Additionally, a considerable portion of iron oxide, hematite (Fe_2O_3, PDF 01-085-0987), as well as minor phases of zirconium oxide, baddeleyite (ZrO_2, PDF 00-013-0307), were detected. The SEM micrographs of the minireactor revealed that the surface is entirely covered by a thin layer of crystals of various size mainly composed of zirconium oxide as shown in Figs. 9a-9g.

After reaction with clay minerals and ZrO^{2+} at 300ºC for 4.5 days, no changes were observed with respect to the previous sample in the XRD pattern (Fig. 8b); the dominant species remain the austenitic metallic matrix of the steel and iron oxide

(Fe_2O_3). In the latter, the diffraction lines are less intense than those observed in the treated reactor without FEBEX. The baddeleyite signals remain also poorly intense. As can be seen from the SEM micrographs (Fig. 9b), the steel surface is covered by a thin layer of fine-grain oxide composed mainly of zirconium oxide as observed in the EDX spectrum, (Fig. 9h). Furthermore, the $K_{\alpha 1}$ lines for Si, Mg and Al arising from clay minerals particles are visible in the associated EDX spectrum. Besides this, some isolated agglomerates together with bright dispersed areas (labelled ① and ② respectively in Figs. 9c-9d) appear over the steel surface (Figs. 9c-9d). According to EDX analysis, the agglomerates were Zr-rich (Fig. 9i), whereas the bright areas were clay minerals rich particles with some zirconium (Fig. 9j) compatible with the ZrO-FEBEX observed by XRD. The SEM cross-sectional analysis (white line in Fig. 10a) only showed the presence of zirconium oxide at the scale-atmosphere interface without its diffusion towards the container which is in agreement with results obtained by EDX surface analysis (Fig. 10b).

Desorption of ZrO^{2+} from the minireactor.

Fig. 8c shows the XRD diffraction pattern of the reactor after the desorption process. The dominant phase was the austenitic pattern arising from the metallic matrix of the steel remains. In addition, some iron oxides and zirconium oxides were detected. These results were similar to those of the post-treatmented reactor which suggests that the reactor did not undergo any structural change.

The morphology of the oxide layer is also similar to that of the reactor after the treatment; the scale is formed by fine–grain oxide crystals over which a few hexagonal crystals are growing, (Figs. 9e-9f). According to EDX analysis (Figs. 9k-9l), the hexagonal crystals (labelled as ④) are of similar composition to that of the small

crystals (labelled as ③) but with higher zirconium content. Furthermore the the $K_{\alpha 1}$ lines for Si, Al and $L_{\alpha 1}$ were detected in the corresponding EDX spectrum which indicated the formation of an insoluble zirconium silico-aluminate. Unfortunately, no phases containing zirconium were identified by cross sectional study because the layer is too thin to be analysed in cross section, therefore no information was provided as can be seen in (Figs. 10c-10d).

Supernatant characterization

The electrochemical properties of the initial solution and supernatant are shown in Table 2. The results showed that the initial pH value decreased from 4.2 to about 2.5 for Sm^{3+}, whereas for ZrO^{2+}, the post-quench pH values before and after hydrothermal treatment remained quasi-alike. In both cases, the pH values indicated an acidic medium of the supernatant solutions. No structural transformation at those acidic conditions was observed in the XRD patterns for the both treated clay minerals (e.g. swelling capacity). That agrees with Lantenois et al. (2005) which observed that the destabilization of smectite in contact with metallic Fe at a pH lower than 7 is not significant. The Pourbaix diagram showed that the E_h and pH values measured for both solutions favour samarium and zirconium as Sm^{3+} and ZrO^{2+} ions respectively in water as ideal solution.

DISCUSSION

As discussed above by XRD and SEM analysis, the interaction between zirconium and FEBEX involved only sorption at the cation-exchange sites located in the interlayer spaces of the clay. Additionally, no evidence of phases appearing as a result

of the chemical interactions of radioactive waste with clay minerals barrier such as zirconium silicates was observed. The generation of these phases is especially important when the suitable properties of the engineered barrier (clay minerals barrier) such as swelling capacity and cation exchange failed to retain the radionuclide. Furthermore, the released iron particles upon container degradation detected by EDX analysis did not provoke a decrease of the swelling properties of the clay mineral. The interaction of ZrO^{2+} with the minireactor was only superficial and no zirconium diffusion towards the metallic container was detected. Moreover, the adsorbed zirconium was retained, even after desorption process (hexagonal crystals) which implies the irreversible participation of the metallic container in the sorption of zirconyl taken as stable uranyl simulator. These findings regarding the active participation of the container in the sorption of ZrO^{2+} under subcritical conditions are in agreement with previous study by Gimenez et al. (2007) who studied the sorption of As(III) and As(V) on different natural iron oxides (hematite, magnetite, and goethite) and found that the hematite showed higher sorption capacity, especially at acidic pH. Additionally, these iron oxide phases have also a relevant role on the retention of radionuclides such as U and Np from the repository and the surrounding rocks, as predicted by Meijer (1990).

Nevertheless, in the case of Sm^{3+}, besides the cation-exchange at the interlayer spaces of the clay, the samarium had also precipitated out of solution to form a solid phase by leaching of cations, mainly sodium or calcium released by ion exchange process. Despite the XRD diffraction pattern did not show any samarium silicate phase provided by the mixed solution of the clay mineral, Sm^{3+} and container; SEM/EDX analysis indicated the generation of an insoluble disilicate phase with a chemical composition compatible with samarium silicate on both the clay minerals and the steel container. Furthermore, the interaction of Sm^{3+} with the minireactor was on the surface

and has not been diffused into the metallic container. This samarium silicate layer remained, but very thin, after desorption process. These findings regarding to the active participation of both components of the engineered barrier in the sorption of Sm^{3+} under subcritical conditions are in contrast to those of Parfitt et al. (1980) who reported that the presence free iron oxides inhibits the sorption by the whole soil. This inhibition was explained by the Fe coating of clay mineral in red earth which suppresses Eu^{3+} sorption. Also, as reported by Wang et al. (2000), these iron oxides in red earth are not a significant sink for Eu^{3+}.

Finally, it is also mentioned that the behaviour of Sm^{3+} is similar to that of Eu^{3+} (El Mrabet et al. 2012). In the case of Eu^{3+}, the amount of europium silicate retained by the container remained even after the desorption process with a thickness of ca. 5 μm, whereas in the case of Sm^{3+}, the samarium silicate layer was too thin to be detected by EDX line profile.

CONCLUSIONS

The main conclusions that can be drawn from the above results are:

- ✓ The interaction between FEBEX and Sm^{3+} involved both sorption at the cation exchange sites located in the interlayer spaces of the clay mineral and the chemical interaction with the generation of an insoluble phase of samarium silicate. In the case of ZrO^{2+}, this interaction revealed only sorption of hydrated cations into the interlayer space.
- ✓ From both studies with Sm^{3+} and ZrO^{2+}, we can deduce that the metallic canister is actively involved in the immobilization of HRW, even during the corrosion process.

ACKNOWLEDGMENTS

We are grateful for financial support from ENRESA (contract nº 0079000121) and from DGICYT and FEDER funds (Projects CTQ2010-14874).

REFERENCES CITED

Alba, M.D., Becerro, A.I., Castro, M.A., and Perdigón, A.C. (2001). Hydrothermal reactivity of Lu-saturated smectites: Part I. A long-range order study. American Mineralogist, 86, 115-123.

Alba, M.D., and Chain, P. (2005). Interaction between lutetium cations and 2:1 aluminosilicates under hydrothermal treatment. Clays and Clay Minerals, 53, 39–46.

Alba, MD., and Chain, P. (2007). Persistence of lutetium disilicate. Applied Geochemistry, 22, 192-201.

Alba, M.D., and Chain, P. (2009). Chemical reactivity of argillaceous material in engineered barrier: Rare earth disilicate formation under subcritical conditions. Applied Clay Science, 43, 369–375.

Allen, C.C, and Wood M.I. (1988). Bentonite in nuclear waste disposal: A review of research in support of the Basalt Waste Isolation Project. Appled Clay Science, 3, 11-30.

Astudillo, J. (2001). El almacenamiento geológico profundo de los residuos radiactivos de alta actividad. Principios básicos y tecnología. ENRESA, Madrid.

Bildstein, O., Trotignon, L., Perronnet, M., and Jullien, M. (2006). Modelling iron-clay interactions in deep geological disposal conditions. Physics and Chemistry of the Earth, 31, 618-625.

Carlson, L., Karnland, O., Oversby, V.M., Rance, A.P., Smart, N.R., Snellma, M., Vähänen, M., and Werme L.O. (2007). Experimental studies of the interactions between anaerobically corroding iron and bentonite. Physics and Chemistry of the Earth, 32, 334-345.

Chain, P. (2007). Estudio del sistema saponita/$Lu(NO_3)_3/H_2O$ en condiciones hidrotermales. Ph.D Thesis Doctoral. University of Seville (Spain).

Chapman, N. (2006). Geological disposal of radioactive waste – concept, status and trends. Journal Iberoamerican Geology, 32, 7-14.

Chapman, A.N., and Smellie J.A.T. (1986). Introduction and summary of the workshop, Chemical Geology, 55, 167-173.

Corma, A., Mifsud, A., and Sanz, E. (1987). Influence of the chemical-composition and textural characteristics of Palygorskite on the acid leaching of octahedral cations. Clay Minerals, 22, 225–232.

Davidtz, J.C., and Low, P.F. (1970). Relation between crystal-lattice configuration and swelling of montmorillonites. Clays and Clay Minerals, 18, 325–332.

Duro, L., El Aamrani, S., Rovira, M., Pablo, J., and Bruno, J. (2008). Study of the interaction between U(VI) and the anoxic corrosion products of carbon steel. Applied Geochemistry, 23, 1094-1100

El Aamrani, S., Gimenez, J., Rovira, M., Seco, F., Grive, M., Bruno, L., Duro, L., and de Pablo J. (2007). A spectroscopic Study of uranium (VI) interaction with magnetite. Applied Surface Science, 253, 8794-8797.

El Mrabet, S., Astudillo, J., Castro, M.A., Hurtado, S., Orta, M.M., Pazos, M.C., Rueda, S., Villa, M., and Alba M.D. (2012) Competitive effect of the metallic canister and clay barrier on the sorption of Eu^{3+} under subcritical conditions, 5th International Meeting on Clay in Natural & Enginerred Barriers for Radioactive Waste Confinement, Montpellier (France).

Fernandez, A., Baeyens, B., Bradbury, M., and Rivas, P. (2004). Analysis of the porewater chemical composition of a Spanish compacted bentonite used in an engineered barrier. Physics and Chemistry of the Earth., 29, 105-118.

Gaudin, A., Gaboreau, S., Tinseau, E., Bartier, D., Petit, S., Grauby, O., Foct, F., and Beaufort, D. (2009). Mineralogical reactions in the Tournemire argillite after in-situ interaction with steels. Applied Clay Science, 43, 196-207.

Gimenez, J., Martínez, M., de Pablo, J., Rovira, M., and Duro L. (2007). Arsenic sorption onto natural hematite, magnetite, and goethite. Journal of the Hazardous Materials 141, 575–580.

Granizo, N., and Missana, T. (2006). Mechanisms of cesium sorption onto magnetite. Radiochimica Acta, 94, 671–677.

Grim, R.E. (1968). Clay Mineralogy. McGraw-Hill Book Company, New York.

Guillaume, D., Neaman, A., Cathelineau, M., Mosser-Ruck, R., Peiffert, C., Abdelmoula, M., Dubessy, J., Villiéras, F., Baronnet, A., and Michau, N. (2003). Experimental synthesis of chlorite from smectite at 300 ºC in the presence of metallic Fe. Clay Minerals, 38, 281–302.

Guillaume, D., Neaman, A., Cathelineau, M., Mosser-Ruck, R., Peiffert, C., Abdelmoula, M., Dubessy, J., Villiéras, F., and Michau N. (2004). Experimental study of the transformation of smectite at 80 and 300 ºC in the presence of Fe oxides. Clay Minerals, 39, 17–34.

Ishidera, T., Ueno, K., Kurosawa, S., and Suyama, T. (2008). Investigation of montmorillonite alteration and form of iron corrosion products in compacted bentonite in contact with carbon steel for ten years. Physics and Chemistry of the Earth 33, S269-S275

Komadel, P., Madejová , J., Janek, M., Gates, W.P., Kirkpatrick, R.J., and Stucki, J.W. (1996). Dissolution of hectorite in inorganic acids. Clays and Clay Minerals, 44, 228–236.

Lantenois, S. (2003). Réactivité fer métal/smectites en milieu hydraté à 80°C. PhD thesis, Université d'Orléans, Orléans, France, pp 188.

Lantenois, S., Lanson, B., Muller, F., Bauer, A., Jullien, M., and Plançon, A. (2005). Experimental study of smectite interaction with metal Fe at low temperature: 1. Smectite destabilization. Clays and Clay Minerals, 53, 597-612.

Malekifarsani, A, and Skachik, M.A., (2009). Calculation of maximum release rates in alternative design changes in the thickness of the buffer for the engineered barrier system (EBS) in deep repository by using Amber code, 51, 355-360.

Mather, J.D., Chapman, N.A., Black, J.H., and Lintern, B.C. (1982). The geological disposal of high-level radioactive waste- a review of the Institute of geological sciences research-program. Nuclear Energy-Journal of the British Nuclear Energy Society, 21, 167-173

McCombie, C., Pentz, D.L., Kurzeme, M., and Miller, I. (2000). Deep geological repositories: a safe and secure solution to disposal of nuclear wastes. In GeoEng2000 – An international conference on geotechnical & geological engineering, 19-24 November 2000. Melbourne, Australia. Lancaster, Technomic.

Meijer, A. (1990). A strategy for the derivation and use of sorption coefficients in performance assessmenct alculations for the Yucca Mountain site. Pg. 9-40. Proceeding of the DOE/yucca Mountain Site Characterization Project Radionuclide Adsorption Workshop at Los Alamos Laboratory. LA 12325~C(NNA.19930629.0011).

Missana, T., Garcia-Gutierrez, M., and Fernandez, V. (2003). Uranium (VI) sorption on colloidal magnetite under anoxic environment: experimental study and surface complexation modelling. Geochimica et Cosmochimica Acta, 67, 2543-2550.

Papillon, F., Jullien, M., and Bataillon C. (2003). Carbon steel behaviour in compacted clay: two long term tests for corrosion prediction. In: Féron, D., MacDonald, D.D. (Eds.), Prediction of the long term corrosion behaviour in nuclearwaste systems. European Federation of Corrosion Publications, vol. 36. Maney Publishing, UK, pp. 439–454.

Parfitt, R.L. (1980). Chemical properties of variable charge soils In: Theng, B.K.G. (ed.). Soils with Variable Charge. New Zealand Soc. Soil Sci., Bureau, Lower Hutt, pp. 167–194.

Perronnet, M. (2004). Réactivité des matériaux argileux dans un contexte de corrosion métallique. Application au stockage des déchets radioactifs en site argileux. PhD Thesis, Institut National Polytechnique de Lorraine, Nancy, France, p 283.

Rebak, R.B. (2006). Selection of Corrosion Resistant Materials for Nuclear Waste Repositories. Report of Lawrence Livermore National Laboratory, UCRL-PROC-221893

Rovira, M., de Pablo, J., Casas, I., Giménez, J., and Clarens, F. (2004). Sorption of caesium on commercial magnetite with low silica content: experimental and modelling. Materials Research Symposium Proceedings, 807, 677–682.

Samper, J., Chuanhe, L., and Montenegro, L. (2008). Reactive transport model of interactions of corrosion products and bentonite. Physics and Chemistry of the Earth, 33, S306–S316.

Savage, D., and Chapman, N.A. (1982). Hydrothermal behaviour of simulated waste glass- and waste-rock ineraction under repository conditions. Chemical Geology, 36, 59-86.

Savage, D., Watson, C., Benbow, S., and Wilson, J., (2010). Modelling iron-bentonite interaction. Applied Clay Science, 47, 91-98.

Smart, N.R., Blackwood, D.J., and Werme, L. (2002). Anaerobic corrosion of carbon steel and cast iron in artificial groundwaters: Part 1 – Gas generation. Corrosion, 58, 627-637.

Tripathy, S., Sriharan, A., and Schanz, T. (2004). Swelling pressure of compacted bentonites from diffuse double layer theory. Canadian Geotechnical Journal, 41, 437-450.

Wang, X.K., Dong, W.M., Li, Z., Du, J.Z., and Tao Z.Y. (2000). Sorption and desorption of radiocesium on red earth and its solid components: relative contribution and hysteresis. Applied Radiation and Isotopes, 52, 813.

Wilson, J., Savage, D., Cuadros, J., Shibata, M., and Ragnarsdottir, K.V. (2006a). The effect of iron on montmorillonite stability. (I). Background and thermodynamic considerations. Geochimica et Cosmochimica Acta, 70, 306-322.

Wilson, J., Cressey, G., Cressey, B., Cuadros, J., Ragnarsdottir, K.V., Savage, D., and Shibata M. (2006b). The effect of iron on montmorillonite stability. (II). Experimental investigation. Geochimica et Cosmochimica Acta, 70, 323-336.

TABLE 1. Chemical composition (w/w %) of the stainless steel AISI 316 L used in this work

Co	V	Si	S	P	Mn	Cr	Fe	Ni	Cu	Mo	Cl
0.14	0.11	0.38	0.03	0.04	1.74	16.53	68.29	10.57	0.29	1.87	0.01

TABLE 2. pH and redox potential (E_h) values of the initial aqueous solution and the solution after hydrothermal reaction at 300ºC for 4.5 days of FEBEX in contact with a $7.9x10^{-2}$ M solution of Sm^{3+} and ZrO^{2+}.

Solution	Sm^{3+}		ZrO^{2+}	
	pH	E_h (mV)	pH	E_h (mV)
Initial	4.20	439	1.38	554
Final	2.47	547	1.55	614

FIGURE CAPTIONS

FIGURE 1. XRD diffraction patterns of the FEBEX smectite: a) Untreated FEBEX. b) After being treated hydrothermally at 300ºC for 4.5 days with a solution of $7.9x10^{-2}$ M Sm^{3+}. q=quartz (PDF 04-006-1757), c=cristobalite (PDF 04-008-7824), h=$H_2Si_2O_5$ (PDF 00-050-0439), and, n=nacrite 2M2 (PDF 01-072-2206).

FIGURE 2. SEM micrograph of: a) the original FEBEX. b) General view of the treated FEBEX at 300ºC for 4.5 days in contact with a solution of $7.9x10^{-2}$ M Sm^{3+}.c) Other zone from b) where block morphology, marked with ①, are shown. EDX spectra of: d) the original FEBEX; (e) EDX of lamellar particles shown in b) after hydrothermal reaction at 300ºC for 4.5 days with a solution of $7.9x10^{-2}$ M Sm^{3+}. f) EDX of block morphology shown in fig. c)

FIGURE 3. XRD diffraction patterns of the minireactor after hydrothermal treatment at 300ºC in contact with a solution of $7.9x10^{-2}$ M Sm^{3+} for 4.5 days: a) without FEBEX b) with FEBEX. c) After desorption process.

FIGURE 4. SEM Micrographs of the minireactor after hydrothermal reaction at 300ºC for 4.5 days in contact with a solution of $7.9x10^{-2}$ M Sm^{3+}: a) General view. b-c) with FEBEX. d-e) after desorption. EDX of different zones viewed in SEM micrographs: f) EDX of the steel as-made. g) After hydrothermal reaction at 300ºC for 4.5 days in contact with a solution of $7.9x10^{-2}$ M Sm^{3+}. h-i) in presence of FEBEX. j-k) After desorption process.

FIGURE 5. a) SEM micrographs of a transverse section of the minireactor after hydrothermal reaction at 300ºC for 4.5 days with FEBEX and a solution of $7.9x10^{-2}$ M Sm^{3+}. b) Intensity profile of the elemental composition. c-d) after desorption process

FIGURE 6. XRD diffraction patterns of the FEBEX smectite: a) Untreated FEBEX. b) After being treated hydrothermally at 300ºC for 4.5 days with a solution of $7.9x10^{-2}$ M ZrO^{2+}. q=quartz (PDF 04-006-1757), and, c=cristobalite (PDF 04-008-7824).

FIGURE 7. SEM micrographs of the treated FEBEX at 300ºC for 4.5 days with a $7.9x10^{-2}$ M solution of ZrO^{2+}: a) A general view; b) bright particles agglomerates constituted mainly of zirconium; and; c) iron particles arising from container degradation. EDX spectra of: d) lamellar particles shown in a) after hydrothermal reaction at 300ºC for 4.5 days with a solution of $7.9x10^{-2}$ M of ZrO^{2+}; e) zirconium agglomerates shown in b); f) EDX of iron particles shown in c); and; EDX spectrum of FEBEX has been included as reference.

FIGURE 8. XRD diffraction patterns of the minireactor after hydrothermal treatment at 300 ºC in contact with a $7.9x10^{-2}$ M solution of ZrO^{2+} for 4.5 days: a) without FEBEX b) with FEBEX. c) After desorption process.

FIGURE 9. SEM Micrographs of the minireactor after hydrothermal reaction at 300ºC for 4.5 days in contact with a $7.9x10^{-2}$ M solution of ZrO^{2+}: a) General view. b-d) in presence of FEBEX. e-f) after desorption process. g-l) The corresponding EDX spectra.

FIGURE 10. a) SEM Micrographs of a transverse section of the minireactor after hydrothermal reaction at 300ºC for 4.5 days with FEBEX and a solution of $7.9x10^{-2}$ M ZrO^{2+}. b) Intensity profile of the elemental composition. c-d) after desorption process.

FIGURE 11. pH-Redox potential (Eh) plot (Pourbaix diagrams) of the initial solution (circle) and the supernatant recovered after hydrothermal treatment(triangle) for :a) $7.9x10^{-2}$ M Sm^{3+} , b) $7.9x10^{-2}$ M ZrO^{2+}.

Fig. 1

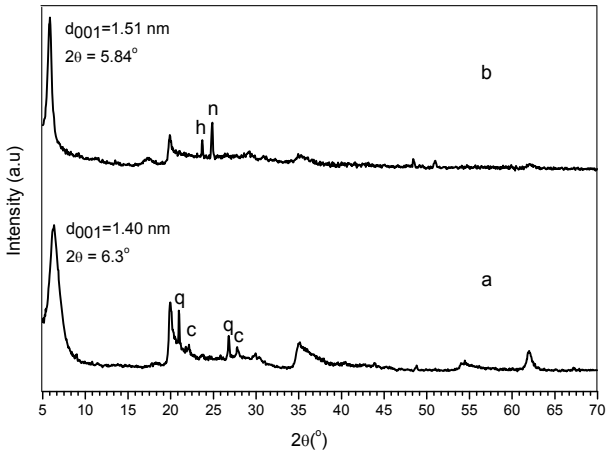
d001=1.51 nm
2θ = 5.84°
b
n
h
d001=1.40 nm
2θ = 6.3°
a
q
c
q
c
Intensity (a.u)
5
10
15
20
25
30
35
40
45
50
55
60
65
70
2θ(°)

Fig. 2

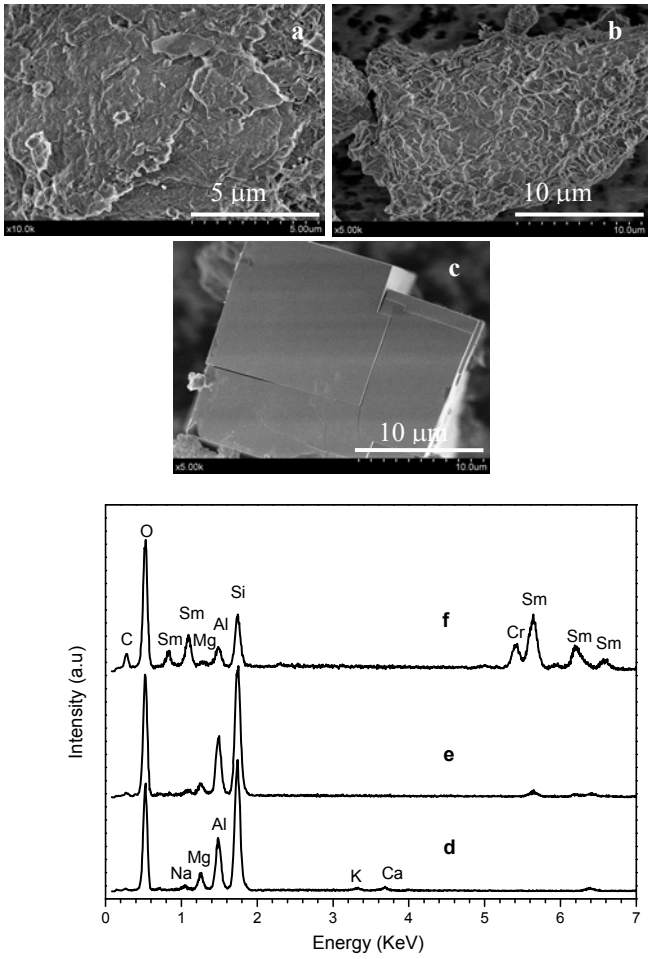
a
5 μm
b
10 μm
c
10 μm
O
C
Sm
Mg
Al
Si
Sm
f
Cr
Sm
Sm
e
Al
Mg
Na
d
K
Ca
Intensity (a.u)
0
1
2
3
4
5
6
7
Energy (KeV)

Fig. 3

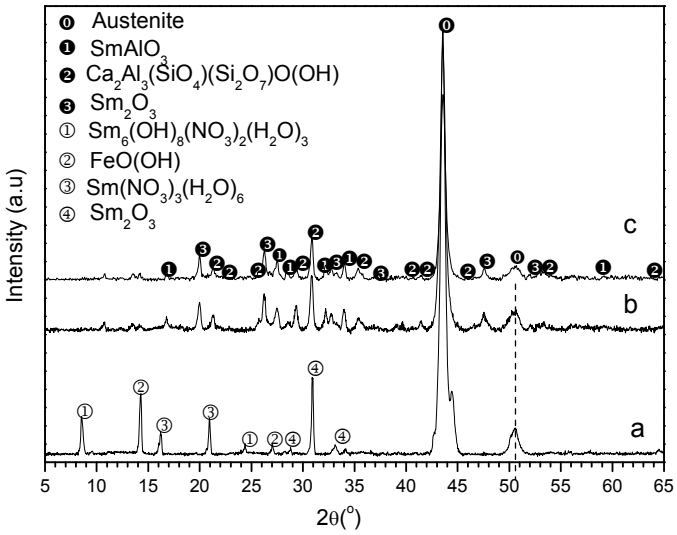
❶ Austenite
❶ SmAlO3
❷ Ca2Al3(SiO4)(Si2O7)O(OH)
❸ Sm2O3
① Sm6(OH)8(NO3)2(H2O)3
② FeO(OH)
③ Sm(NO3)3(H2O)6
④ Sm2O3
Intensity (a.u)
2θ(°)
c
b
a
5 10 15 20 25 30 35 40 45 50 55 60 65

Fig.4

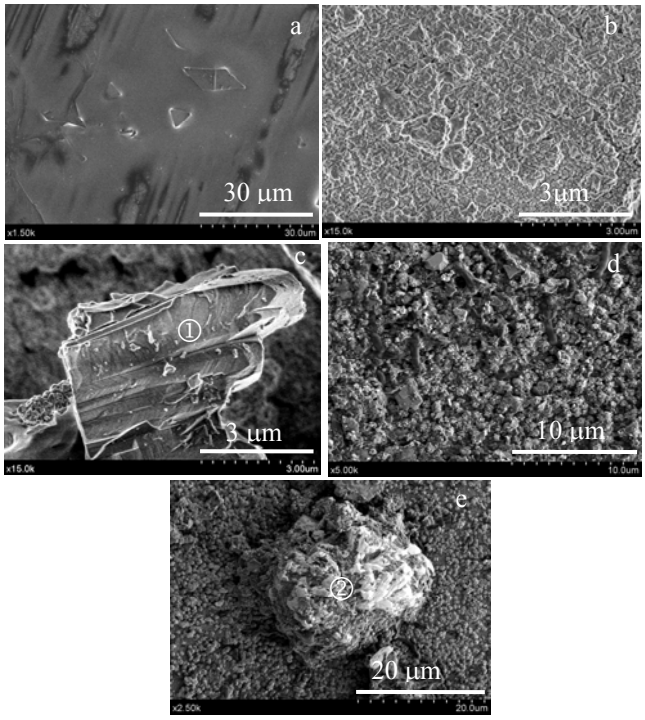
a
30 μm
b
3μm
c
①
3 μm
d
10 μm
e
②
20 μm

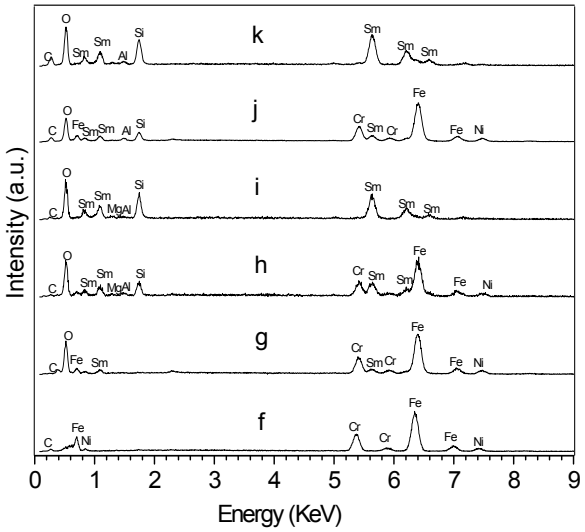
k
j
i
h
g
f
O
Si
Sm
Al
C
Fe
Ni
Cr
Mg
Intensity (a.u.)
0 1 2 3 4 5 6 7 8 9
Energy (KeV)

Fig. 5

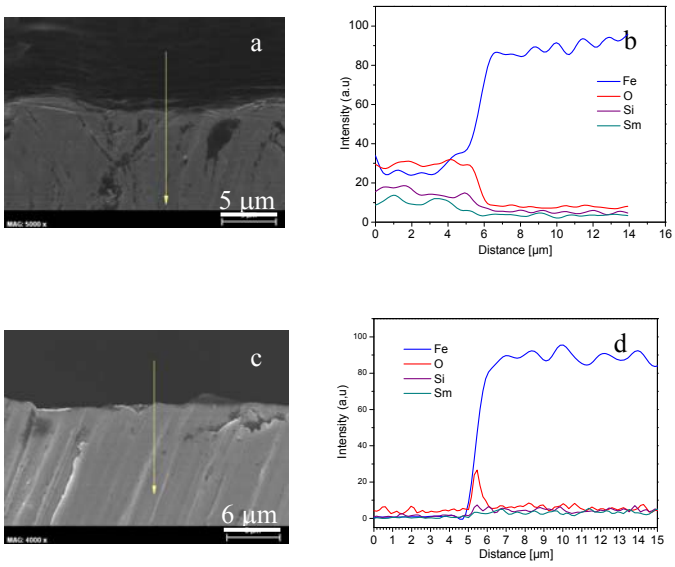
a
5 µm
b
Fe
O
Si
Sm
Intensity (a.u)
Distance [µm]
c
6 µm
d
Fe
O
Si
Sm
Intensity (a.u)
Distance [µm]

Fig. 6

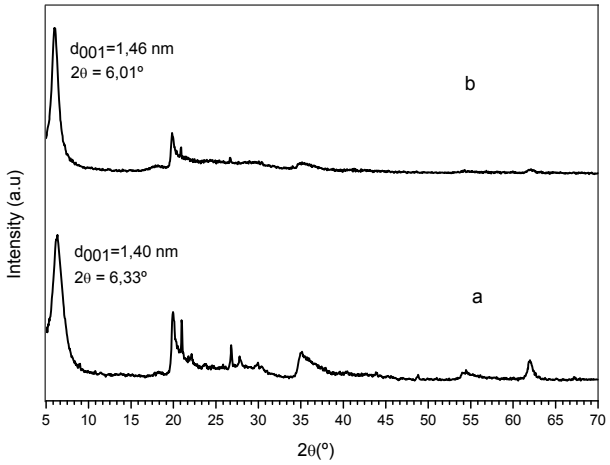
d001=1,46 nm
2θ = 6,01º
b
d001=1,40 nm
2θ = 6,33º
a
Intensity (a.u)
5
10
15
20
25
30
35
40
45
50
55
60
65
70
2θ(º)

Fig. 7

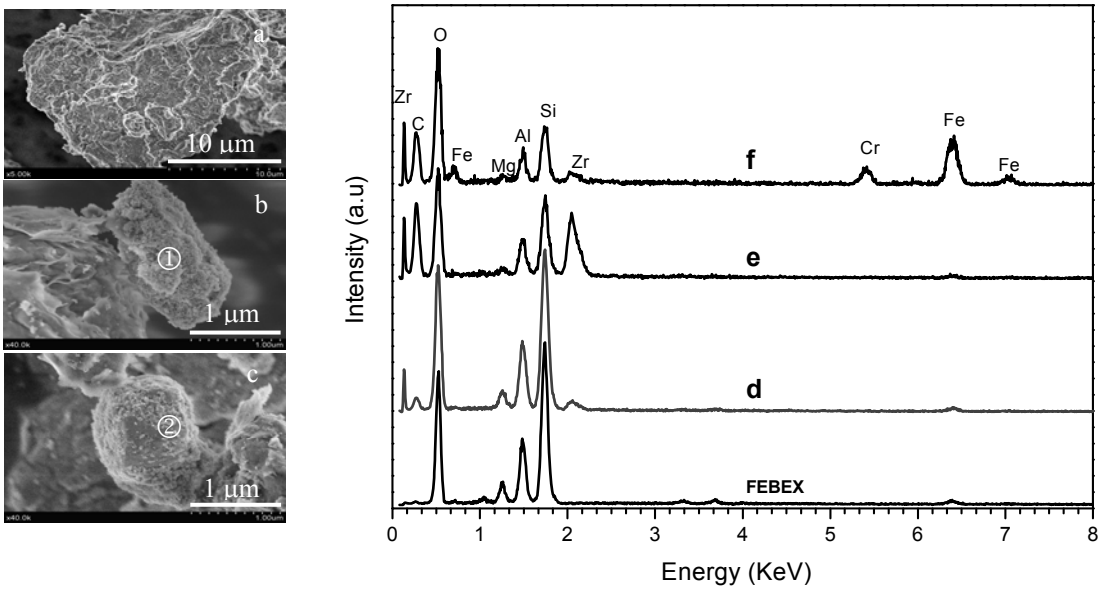
a
10 μm
b
①
1 μm
c
②
1 μm
Intensity (a.u)
O
Zr
C
Fe
Mg
Al
Si
Zr
f
Cr
Fe
Fe
e
d
FEBEX
0
1
2
3
4
5
6
7
8
Energy (KeV)

Fig. 8

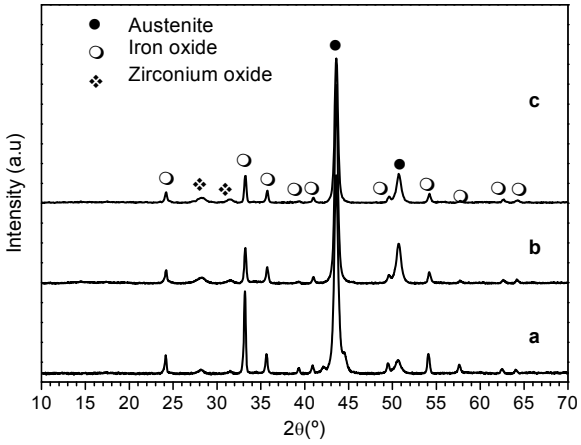
Austenite
Iron oxide
Zirconium oxide
c
b
a
Intensity (a.u)
10 15 20 25 30 35 40 45 50 55 60 65 70
2θ(°)

Fig. 9

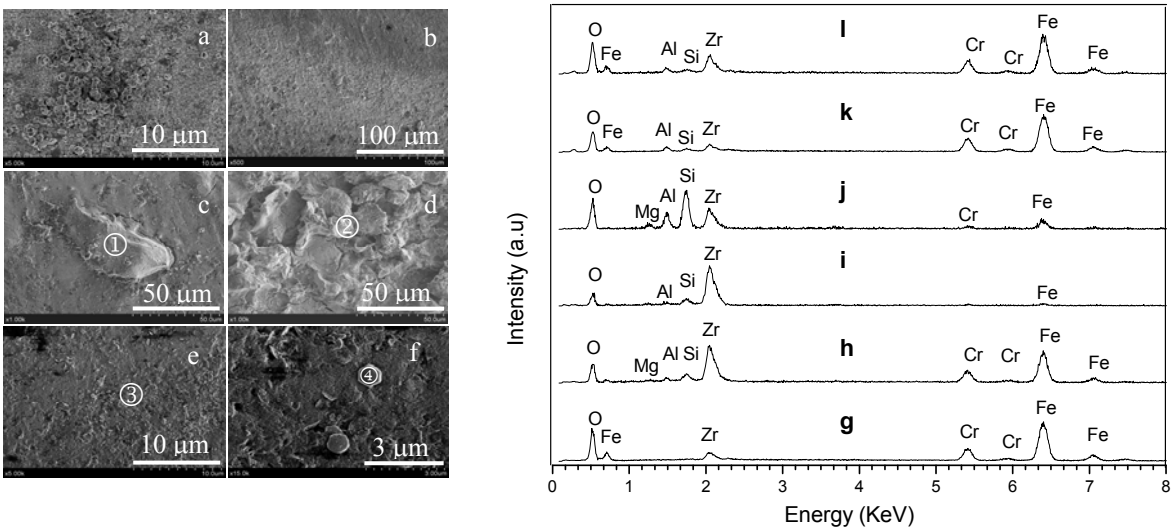
a
10 μm
b
100 μm
c
①
50 μm
d
②
50 μm
e
③
10 μm
f
④
3 μm
Intensity (a.u)
l
k
j
i
h
g
O
Fe
Al
Si
Zr
Mg
Cr
0
1
2
3
4
5
6
7
8
Energy (KeV)

Fig. 10

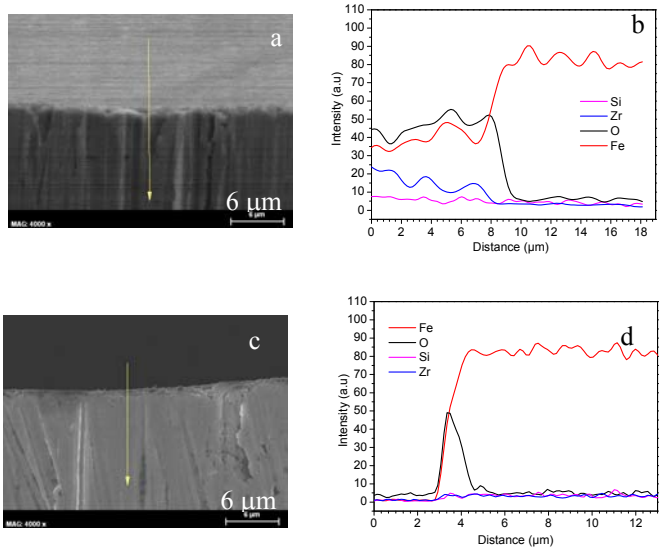
a
6 µm
b
Intensity (a.u)
Distance (µm)
Si
Zr
O
Fe
c
6 µm
d
Intensity (a.u)
Distance (µm)
Fe
O
Si
Zr